

Modeling epitaxial film growth of C_{60} revisited

William Janke and Thomas Speck

*Institut für Physik, Johannes Gutenberg-Universität Mainz, Staudingerweg 7-9, 55128 Mainz, Germany**

Epitaxial films evolve on time and length scales that are inaccessible to atomistic computer simulation methods like molecular dynamics (MD). To numerically predict properties for such systems, a common strategy is to employ kinetic Monte Carlo (KMC) simulations, for which one needs to know the transition rates of the involved elementary steps. The main challenge is thus to formulate a consistent model for the set of transition rates and to determine its parameters. Here we revisit a well-studied model system, the epitaxial film growth of the fullerene C_{60} on an ordered C_{60} substrate(111). We implement a systematic multiscale approach in which we determine transition rates through MD simulations of specifically designed initial configurations. These rates follow Arrhenius' law, from which we extract energy barriers and attempt rates. We discuss the issue of detailed balance for the resulting rates. Finally, we study the morphology of subatomic and multi-layer film growth and compare simulation results to experiments. Our model enables further studies on multi-layer growth processes of C_{60} on other substrates.

I. INTRODUCTION

Layer and cluster growth processes of organic molecules on dielectric or metallic surfaces have gained popularity in science and technology in recent years as a possible gateway to the manufacturing of new electronic structures at the molecular level [1]. As Moore's law for today's silicon-based technology is predicted to flatten out in the near future, technological innovations will be necessary to further improve future electronic devices [2, 3]. Another area is organic photovoltaics [4]. The self-assembly of nanostructures on substrates is a promising strategy [5–8] and requires the understanding and control of growth processes to achieve target aggregate morphologies.

In particular carbon-based architectures such as the fullerene C_{60} have been studied extensively. Morphologies and kinetics of C_{60} film growth has been investigated experimentally on different substrates: graphite [9], pentacene [10], calcium fluoride [11, 12], mica [13], and iron [14]. To access the large time and length scales required to predict morphologies in computer simulations requires coarse-graining. The dynamics of organic molecules on a lattice can be modeled as discrete jumps on time scales much longer than those of molecular vibrations [15]. The effective dynamics is necessarily stochastic and determined by a relatively small number of elementary discrete events. Such a dynamics is simulated efficiently employing the kinetic Monte Carlo (KMC) algorithm [16] (also called Gillespie algorithm [17, 18]). In principle, it requires the knowledge of the rates for all possible events, the determination of which for complex systems is a formidable task if not impossible. For the film growth of C_{60} , KMC simulations with a simplified rate catalogue have been conducted to reproduce experimental observations [12, 13, 19–22].

The number of possible transitions depends on the

choice for the lattice and whether to neglect the distinction between A and B edge steps, which strongly influences cluster shapes [15]. One approach is to assume an Arrhenius law, which requires an attempt rate and an energy barrier for each possible transition. For C_{60} , energy barriers have been calculated from density functional theory (DFT) [23] and molecular mechanics [24].

Setting up a KMC simulation, there is no unique way to determine the involved transition rates. One common approach is to describe the energy barriers and attempt rates through a simple self-consistent model involving a bond counting approach for the energy barriers with very few free parameters that are then either taken from literature or tuned to reproduce some experimental result [12, 13]. However, without independent verification of the validity of those free parameters, the resulting transition rates might be unphysical, or the parameters can lose their intended interpretation. Another approach is to measure energy barriers and attempt rates for the transitions of interest directly, *e.g.*, in MD simulations [19]. However, as systematic or statistical uncertainties may be involved in those measurements, KMC models that make direct use of such transition rates are likely to be thermodynamically inconsistent (*i.e.*, the rates break detailed balance).

Here, we follow a hybrid approach and systematically determine the rates for the deposition and epitaxial growth of C_{60} on a C_{60} (111) surface from off-lattice, coarse-grained molecular dynamics simulations (Fig. 1). We then construct a thermodynamically consistent model for the transition rates that is based on the MD simulation results. Establishing a thorough understanding of this system is crucial as it can then be applied to second layer processes in simulations with other substrates. The outline is as follows: We start by setting up MD simulations of interacting C_{60} molecules to determine attempt rates and energy barriers for elementary transitions involving only a single C_{60} molecule. To enforce the detailed balance condition, we will then reduce the number of parameters yielding a simplified model with 7 parameters, and compare the behavior of this

* Corresponding author: thomas.speck@uni-mainz.de

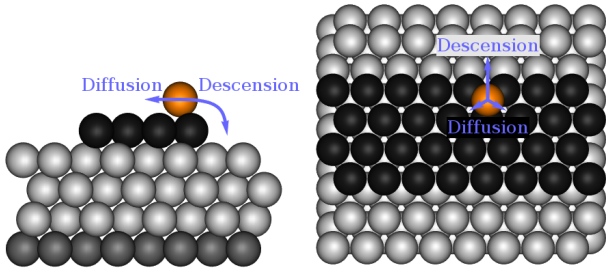


Figure 1. Example MD simulation setup. Right: Top view. Left: Side view. The dark gray particles are fixed in place to ensure an fcc crystal structure with a (111) surface. The three layers of light gray particles are freely evolving during the NVE simulation, but are under the effect of a Langevin thermostat or velocity rescaling at the beginning of the simulation. The black particles are set in a stable configuration where they are unlikely to move and set up the environment for the tagged orange particle, which is set in a state where the transitions of interest can be observed. Both black and orange particles are never under the effect of a thermostat or velocity rescaling. In this example setup, the transitions of interest are the descension and diffusion of the orange particle.

model to the results obtained using the raw MD parameters.

II. METHODS

A. MD Simulations: C_{60} on $C_{60}(111)$

To determine energy barriers and attempt rates for the diffusion of C_{60} on a $C_{60}(111)$ surface, we set up MD simulations using LAMMPS [25]. The interaction between the individual C_{60} molecules is modeled by a classical Girifalco pair potential [26, 27]

$$u(s) = -\alpha \left(\frac{1}{s(s-1)^3} + \frac{1}{s(s+1)^3} - \frac{2}{s^4} \right) + \beta \left(\frac{1}{s(s-1)^9} + \frac{1}{s(s+1)^9} - \frac{2}{s^{10}} \right) \quad (1)$$

with parameters $\alpha = 46.7 \times 10^{-3} \text{ eV}$ and $\beta = 84.5 \times 10^{-6} \text{ eV}$. Here, $s = r/R$ is the center-to-center distance r of the two interacting molecules scaled by the nucleus-to-nucleus diameter of a C_{60} molecule, $R = 0.71 \text{ nm}$. This potential yields a potential minimum of $E_G = 277 \text{ meV}$ at a center-center distance of $r_{\min} = 1.005 \text{ nm}$. Precision measurements show a very good agreement of this potential with experimental forces [28]. Still, one has to keep in mind that this coarse-grained potential removes rotational degrees of freedom as well as vibrations/deformations from the C_{60} molecules, which can potentially play a role in the transition paths.

The C_{60} substrate is modeled by four layers of which the bottom layer is immobilized. On top of the substrate, a stable configuration of deposited particles is set

up with one or a few tagged particles left in metastable states. The life time of these metastable states as well as the frequency of outgoing transition types are observed to determine the associated transition rates. An example setup of such an MD simulation is shown in Fig. 1. To initialize the system to a random starting configuration at a given temperature, a combination of the Langevin thermostat and velocity rescaling is applied. After equilibration, distributions of life times are obtained in NVE simulations.

B. KMC Simulations

In order to simulate at the length and timescales necessary for the observation of epitaxial growth processes, we employ a kinetic Monte Carlo (KMC) simulation. We implement two superimposed triangular sublattices with a lattice constant of $a = 1 \text{ nm}$ corresponding to the van der Waals diameter of C_{60} [29]. A second layer with the same geometry can also be occupied as soon as a cluster has formed that can support it. A visualization of the lattice geometry can be found in Fig. 2a. The basic types of implemented transitions are shown in Fig. 2b.

The deposition of particles is part of the KMC rate catalogue and occurs randomly with a deposition rate $k_{\text{Dep}} = FA$, where A is the system area in nm^2 . The molecular flux F is set to a constant value of $5 \times 10^{-4} \text{ nm}^{-2}\text{s}^{-1}$. The x and y coordinates of deposition are picked randomly, and deposition can also occur directly onto the second layer of a cluster. If the target location is not valid (because the first layer is already taken and the second layer is either also taken or not sufficiently supported by particles below) a random walk is initiated at the target location to find a valid location for deposition in the proximity. Particles with more than four lateral neighbors are considered immobile in our simulation, while particles with one to four lateral neighbors have the possibility to move either by edge diffusion, ascension, descension, or dissociation. Furthermore, there are two types of edge diffusion transitions with different transition rates that have to be distinguished: edge diffusion along A step and along B step edges (see Fig. 2c for a visualization of the distinction between the two). The transition rates of all these possible transitions have to be modeled and the model parameters will be determined using the data from MD simulations.

III. RESULTS

A. MD Simulations

We ran many simulations at several different temperatures T in the range between 200 K up to 850 K and measure the total time the tagged particle has spent in the initial state at each temperature, $t_{\text{tot}}(T)$, as well as the number of occurrences of each transition of interest,

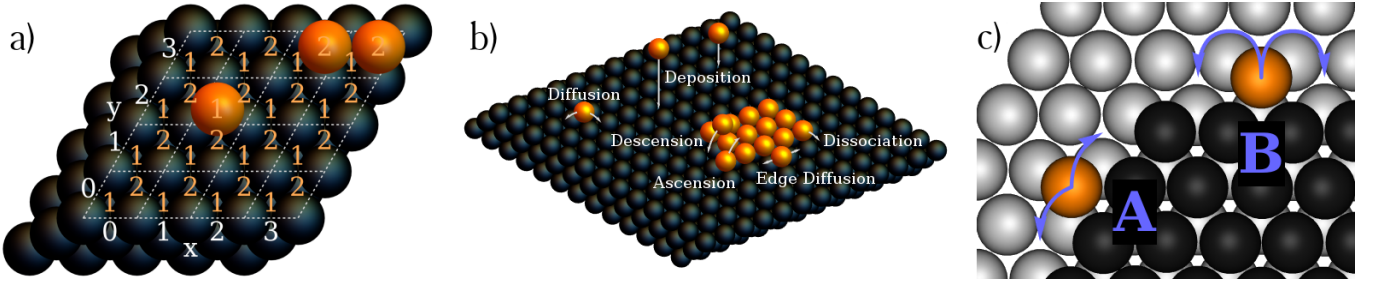


Figure 2. Geometry and involved transition types. (a) Visualization of the sublattices. The unit cell is a parallelogram with two sublattice positions. A freely diffusing particle always jumps from one sublattice to the other, and particles that belong to the same cluster always occupy the same sublattice. Periodic boundary conditions are applied to x and y direction, while the z direction consists of two layers. (b) Visualization of the transition types in the simulated system. (c) Difference between A and B step edge diffusion. While on A step edges, the orientation of the base layer facilitates the edge diffusion transition, on B step edges it does not. As a result, dissociation and reassociation can be the more probable trajectory at B step edges.

$n_\alpha(T)$. The transition rates for every transition α are estimated through

$$k_\alpha(T) \approx \frac{n_\alpha(T)}{t_{\text{tot}}(T)}. \quad (2)$$

The transition rates $k_\alpha(T)$ are then fitted with an Arrhenius law to obtain an energy barrier ΔE_α and an attempt rate ν_α for the transition α . The configurations investigated are visualized in Table I along with the possible transition targets as well as their corresponding energy barriers and attempt rates, which are obtained from Arrhenius plots. Example Arrhenius plots for two of the configurations are given in Fig. 3. In the following, when one of the transitions of Table I is referred to, the reference will be comprised of the label on the image and the roman number of the transition target (*e.g.* (F)I for the free diffusion transition).

In comparison to previous estimates we find that our

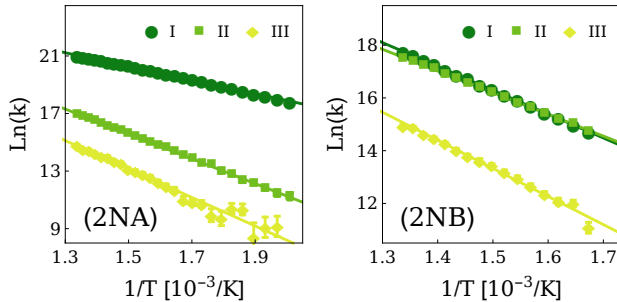


Figure 3. Example Arrhenius plots. The temperature range is varied depending on the configuration in order to observe as many transitions as possible. Left: Configuration (2NB) of table I with a temperature range of $T \in [600, 750]$ K, sampling a total of ≈ 120000 trajectories. Right: For configuration (2NA) with a temperature range of $T \in [500, 750]$ K, sampling a total of ≈ 2300000 trajectories. Because in configuration (2NA) transition I had a much higher transition rate than the transitions II and III, a much larger amount of trajectories was needed to sufficiently sample all transitions.

value for the free diffusion barrier of $E_D = 195.6(20)$ meV falls between the values obtained previously: Graviil *et al.* [30] (168 meV, pair potential calculations), Liu *et al.* [19] (178(4) meV, MD simulations), Cantrell and Clancy [24] (205(22) meV, molecular mechanics), and Goose *et al.* [23] (207 meV, DFT calculations). In Table II, we compare our values for energy barriers to available previous results. To get an estimate for the Ehrlich-Schwöbel barrier of this system, we have to subtract the free diffusion barrier from the energy barrier for descension given by (ES)II,

$$E_{ES} = E_{DES} - E_D \\ = 300.2 \text{ meV} - 195.6 \text{ meV} = 104.6(24) \text{ meV}, \quad (3)$$

which is in very good agreement with the estimate by Goose [23] of 104 meV.

B. Modeling the rates

All rates measured in the MD simulations conform with the Arrhenius law so that we split transition rates $k = \nu e^{-\Delta E/k_B T}$ into attempt rate ν and energy barrier ΔE , both of which are independent of temperature. Since the interaction between C_{60} molecules is short-ranged (see appendix A), we simplify rates by assuming that they only depend on the initial state and the type i of transition but not on the target state. We thus arrive at the parametrization

$$k_i(n, T) = \nu_i(n) e^{-\Delta E_i(n)/k_B T} \quad (4)$$

characterizing the initial state by the number n of neighbors in the same layer. The possible types i are D (free diffusion and dissociation), EDA (edge diffusion along A steps), EDB (edge diffusion along B steps), A (ascension), and DES (descension).

In Fig. 4, the energy barriers extracted from the MD results are plotted as a function of initial neighbors. We

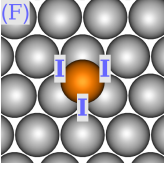
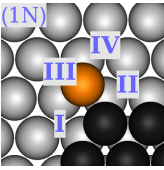
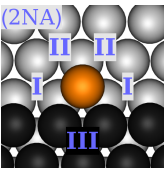
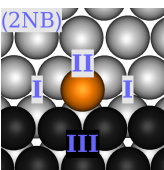
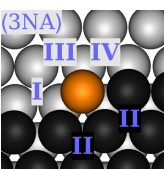
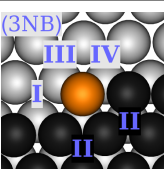
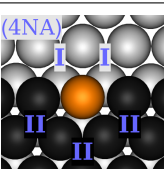
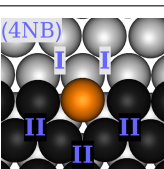
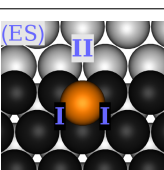
Configuration	T	Jump to	ΔE [meV]	ν_0 [10^{12} Hz]
 (F)	200	I	195.6(20)	0.43(4)
	—			
	380			
	K			
 (1N)	350	I	501(4)	0.53(6)
	—	II	188.3(6)	0.262(4)
	550	III	409(2)	0.38(2)
	K	IV	458(4)	0.25(4)
 (2NA)	500	I	439(2)	0.74(3)
	—	II	744(5)	1.23(12)
	750	III	879(34)	2.29(144)
	K			
 (2NB)	600	I	779(5)	4.60(38)
	—	II	708(4)	2.46(18)
	750	III	917(29)	5.33(266)
	K			
 (3NA)	680	I	686(5)	1.33(10)
	—	II	1119(30)	4.32(210)
	770	III	1037(20)	4.55(148)
	K	IV	1062(24)	6.29(165)
 (3NB)	680	I	989(17)	3.01(82)
	—	II	1119(24)	4.76(186)
	770	III	967(13)	3.49(73)
	K	IV	618(9)	0.20(3)
 (4NA)	750	I	906(12)	0.91(16)
	—	II	1295(46)	2.47(169)
	840			
	K			
 (4NB)	750	I	1270(18)	10.4(28)
	—	II	1311(39)	3.83(217)
	840			
	K			
 (ES)	250	I	181.4(3)	0.325(3)
	—	II	300.2(13)	0.385(18)
	400			
	K			

Table I. Summary of the results from our MD Simulations. The first column shows the configuration with tagged particle (orange) and the possible transitions (blue numerals).

Transition	our work	MM [24]	MD [19]
(F)I	195.6(20)	205(22)	178(4)
(1N)III	409(2)	448(25)	429(57)
(2NB)II	708(4)	717(29)	-
(ES)II	300.2(13)	334(20)	-

Table II. Comparison of energy barriers ΔE (in meV) with previous results from molecular mechanics (MM) and molecular dynamics (MD). Note that the MM results are consistently larger.

observe a linear dependence, which motivates to further parametrize the energy barriers as

$$\Delta E_i(n) = E_i + \hat{n}_i E_{B,i}. \quad (5)$$

Here, E_i is a base energy barrier and $E_{B,i}$ is an effective bond energy for transitions of type i . For dissociation and the descension to the lower layer, $\hat{n}_i = n$ is equal to the number of initial lateral neighbors n . However, for edge diffusion and ascension transitions lateral bonds can be sustained during the transition, which leads to $\hat{n}_i = n - 1$ for edge diffusion and $\hat{n}_i = n - 2$ for ascension.

From the linear fits in Fig. 4 we can extract the effective bond energies $E_{B,i}$ for the different transition types, which are listed in Table III. The Girifalco potential we use in the MD simulations has an energy minimum of $E_G = 277$ meV, which is what we would expect as an energy barrier whenever a bond has to be broken completely to go through a transition. For the case of dissociation, the effective bond strength is in very good agreement

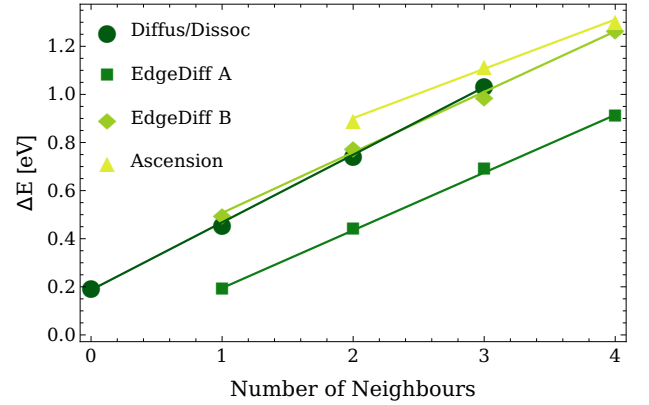


Figure 4. Energy barriers of the different transition types plotted against the number of initial neighbors. The dissociation barriers are taken from (1N)IV, (2NA)II and (3NA)III, which are the longer dissociation paths compared to the ones in B step directions and are therefore the energy barriers for a complete dissociation. For the energy barriers of ascension there is no significant difference between the A step and B step case, so we took the average of the two respective measurements for this plot. The data for edge diffusion along an A step edge is comprised of (1N)II, (2NA)I, (3NA)I and (4NA)I, while edge diffusion along a B step edge is given by (1N)I, (2NB)I, (3NB)I and (4NB)I. All energy barriers are well described by linear fits (lines).

Transition type i	$E_{B,i}$ [meV]	E_i [meV]
diff./dissociation D	276(5)	192(6)
A edge step EDA	245(4)	190(5)
B edge step EDB	254(10)	508(13)
ascension A	206(12)	901(14)
descension Des	276(5)	300(1)

Table III. Fitted effective bond energies $E_{B,i}$ and base energy barriers E_i , cf. Eq. (5).

with this assumption as E_G is very close to our fit value of $E_{B,D}$. The effective bond strengths of edge diffusion along A and B step edges overlap within their margins of error and are both significantly lower than the full bond energy E_G . This was also expected as the transitional states of the edge diffusion transitions are mostly still close enough to the initial neighbors such that the transitioning molecule does not have to overcome the total bond energy in order to slide down into the target state. This implies that the assumption of short-ranged interaction and transition rates that only depend on the nearest neighbor configuration is not entirely valid and has to be seen as an approximation in our KMC simulations. The significantly lower effective bond strength of the ascension transition of only 205(10) meV per bond was unexpected and at this point is not completely understood. An analysis of the exact transition paths of ascension may lead to interesting insights but is not performed in this work since the ascension transitions have a high enough energy barrier to not play a big role in the following KMC simulations. We have not set up an extra set of simulations to determine the effective bond strength $E_{B,DES}$ for descension transitions, so we assume that it is equal to $E_{B,D}$ as it also has a long transition path in which all initial bonds have to be overcome.

The base energy barriers E_i obtained from the fits of Fig. 4 and from the MD simulation for descension are listed in Table III. The fact that edge diffusion along an A step edge is initialized by a transition path very similar to the free diffusion transition results in a base energy barrier E_{EDA} that is close to the free diffusion barrier E_D . The base energy barrier for edge diffusion along B step edges is significantly larger than for the A step case, which is important for the formation of the triangular star shaped clusters that have been observed in experiments [9, 11]. These star shapes evolve because of two effects that stem from the difference of A and B

Transition type i	n				
	0	1	2	3	4
diff./dissociation D	0.43	0.25	1.23	4.02	-
A edge step EDA	-	0.26	0.74	1.33	0.91
B edge step EDB	-	0.53	4.60	3.01	10.4
ascension A	-	-	3.81	4.54	3.15
descension Des	0.38	0.38	0.38	0.38	0.38

Table IV. Effective attempt rates $\nu_{i,n}$ as a function of neighbors n used in the RawMD simulations (in units of THz).

step barriers. First, the higher mobility at A step edges increases the chance of finding a state with high coordination, while particles on B step edges are likely to stick to an initial site with low coordination. Secondly, when particles reach a “corner” state [see (1N) and (3NA)/(3NB) in Tab. I] they are more likely to transition into the direction of an A step edge. As a result, trajectories from A step to B step edges are less likely to occur than from B step to A step edges. Since an ascending molecule has to overcome almost the full adsorption energy, the base energy barrier E_A is almost equal to the adsorption energy of C₆₀ on C₆₀(111), which is around 930 meV (calculated with the Girifalco potential at zero Kelvin).

The attempt rates do not show any specific behavior in terms of the number of initial neighbors so we do not describe them with a model and just take the values as measured in the MD simulations. The exact values of the attempt rates $\nu_{i,n}$ are provided in Table IV.

In the following KMC simulations, we will consider two model variants. The first one (termed “RawMD” model) is given by the energies and attempt rates just described. In addition, we consider a further simplified version (the “Simple” model), where we only use one free attempt rate parameter $\nu_i(n) = \nu_0$. The second distinction between the two models is made with respect to the effective bond strengths $E_{B,i}$. In the “RawMD” model we allow for the transition types to have different effective bond strengths as we have measured slight differences in MD simulations. In the “Simple” model we discard these differences and demand that all transitions scale with the same effective bond strength $E_{B,i} = E_B$. In summary, for the “RawMD” model we end up with 23 parameters for attempt rates and 10 for energy barriers, while the “Simple” model only has one parameter for attempt rates and 6 for energy barriers.

C. KMC Simulations

1. Detailed balance

One important aspect of extracting rates from MD simulations is their thermodynamic consistency. The atomistic dynamics is derived from a Hamiltonian and thus obeys detailed balance guaranteeing the absence of (steady) dissipation. For the KMC simulations, the detailed balance condition can be expressed as $p_C k_{C \rightarrow C'} = p_{C'} k_{C' \rightarrow C}$, where C is a configuration (the position of all molecules), p_C is the stationary probability to observe this configuration, and $k_{C \rightarrow C'}$ are the transition rates to go from one configuration to another. Possible transitions are $k_i(n)$, cf. Eq. (4). The question is whether these rates with the extracted parameters obey detailed balance.

A simple and practical way to test this condition is to calculate the stochastic entropy production [31]. To this end, we prepare a small 10×10 unit cell system at a temperature of $T = 318$ K without deposition and with nine

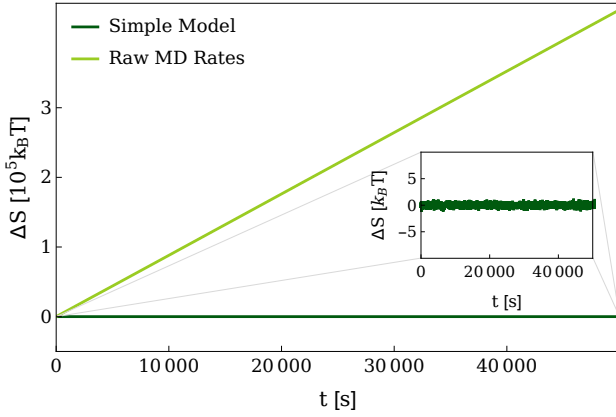


Figure 5. Comparison of the average entropy production between the RawMD and Simple model plotted against time t . The ensemble average is calculated from 100 trajectories at a temperature of $T = 318$ K.

particles assembled into a cluster. During the simulation, the particles of this cluster will evolve through the different transition types in various successions and we can observe if any net entropy production occurs. After every KMC step, we calculate the change of (dimensionless) entropy

$$\delta s = \ln \frac{k_i(n)}{k_j(m)} \quad (6)$$

as the logarithm of the ratio between the rate $k_i(n)$ of the transition that occurred (the new number of neighbors is m) and the rate $k_j(m)$ of the transition that would reverse the KMC step. Summing up these single contributions along a trajectory yields the total entropy production ΔS . After some initial relaxation, this total entropy production should fluctuate around zero if detailed balance were to be obeyed. As shown in Fig. 5, this is not the case for the RawMD model, which exhibits a linear increase corresponding to a substantial dissipation of $8.81k_B T$ of entropy per second. In contrast, our Simple model does obey detailed balance as demonstrated in Fig. 5. This demonstrates that simply transferring rates from MD simulations is likely to break detailed balance and thus yield a thermodynamically inconsistent model, which can lead to severe artifacts.

2. Morphologies

To compare the emerging cluster morphologies of the two models, KMC simulations are conducted in a temperature range of 225 – 360 K with a system size of $A \approx 0.866 \mu\text{m}^2$ (1000 times 1000 unit cells of size 0.886 nm^2). The system starts with an empty lattice and deposition of particles proceeds until a coverage of 10% is reached. This deposition phase takes about $t_D \approx 230$ s to complete. The simulation then continues without deposition to enable relaxation of the clusters for another $t_R \approx 460$ s.

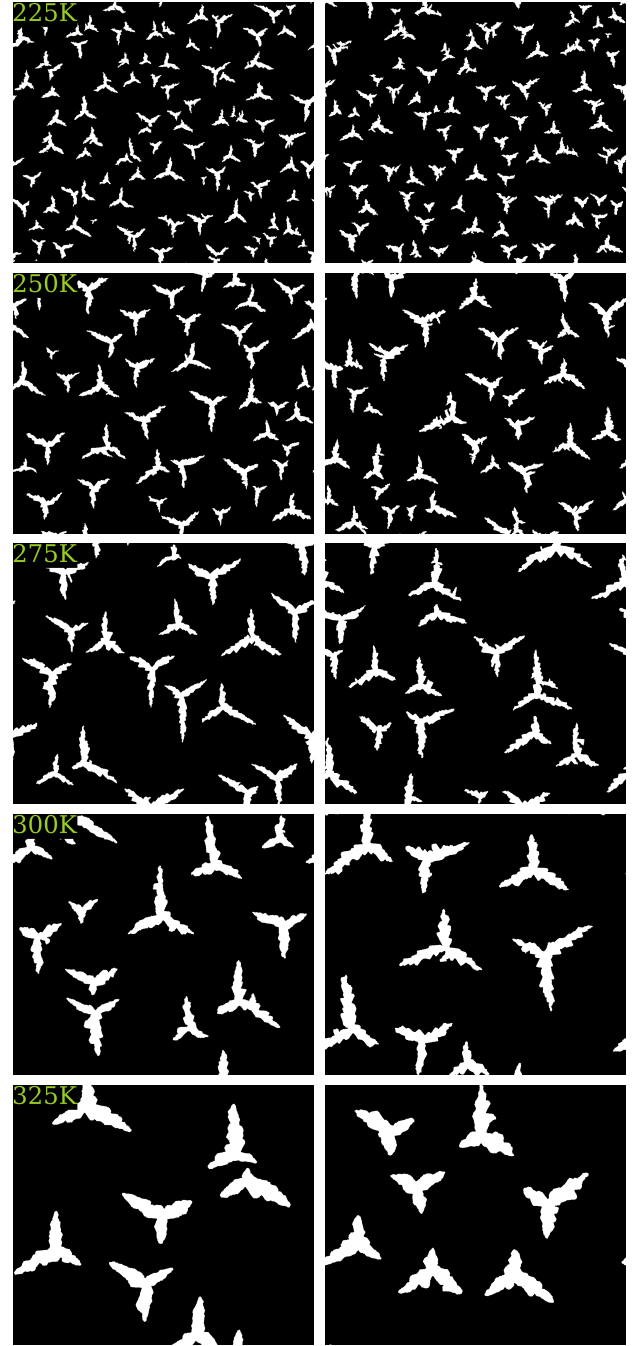


Figure 6. KMC simulation snapshots of RawMD (left) and Simple (right) model at several temperatures (increasing from top to bottom). Parameters for the Simple model are $E_B = 235$ meV and $\nu_0 = 0.25$ THz. The snapshots show an area of $1000 \text{ nm} \times 866 \text{ nm}$ and each contains 100000 molecules corresponding to 10% coverage.

Figure 6 shows representative snapshots for five different temperatures. With the bare eye, no significant differences between the snapshots of the RawMD and Simple model can be spotted.

To compare the morphologies of the different models more quantitatively, three geometric properties of the

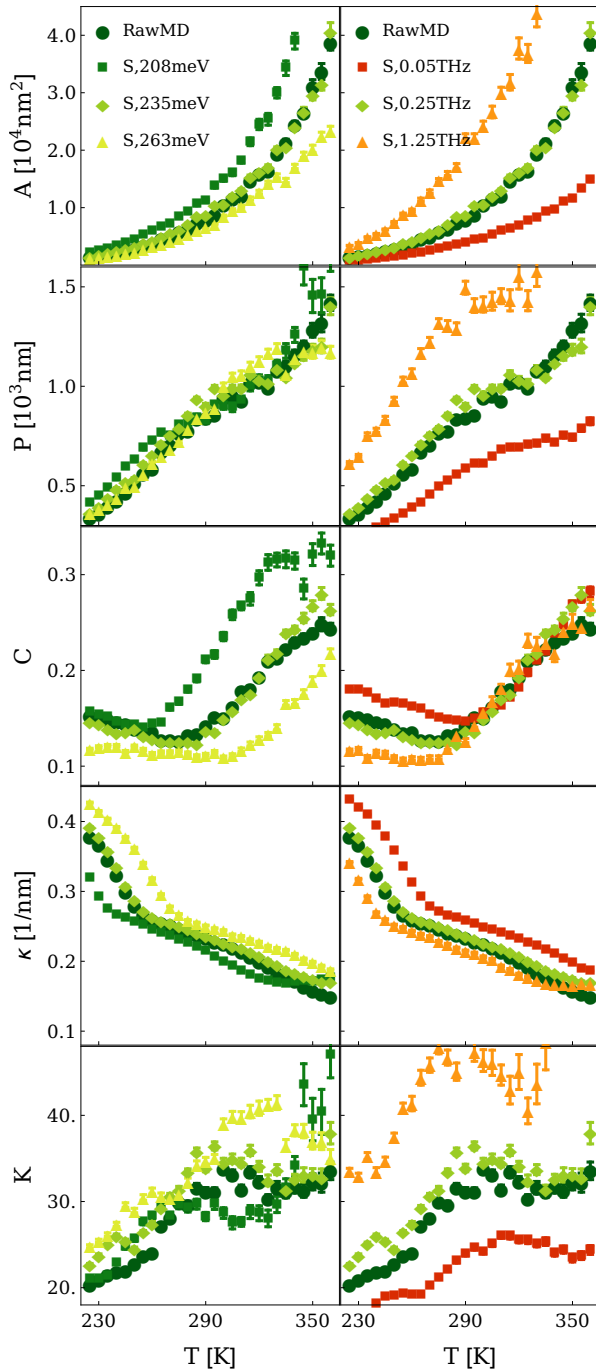


Figure 7. Average cluster features of the two KMC models in a temperature range from 225 K to 360 K. Left: Comparison of the RawMD Model to three Simple models with varying effective bond strength E_B and a constant attempt rate of $\nu_0 = 0.25$ THz. Right: Comparison of the RawMD Model to three Simple models with varying attempt rate ν_0 and a constant effective bond strength of $E_B = 235$ meV. As suggested by the shape descriptors, the resulting cluster morphologies are very similar.

arising clusters are measured: The covered area A , the perimeter P and the mean border curvature $\bar{\kappa}$. Area

and perimeter are directly calculated from the number of molecules in the cluster N and the number of molecules at its edge N_E via

$$A = N \times 0.866 \text{ nm}^2, \quad P = N_E \times 1 \text{ nm}. \quad (7)$$

Details for the calculation of $\bar{\kappa}$ are found in appendix B. We also determine two dimensionless quantities, the circularity C and the dimensionless curvature K defined through

$$C = \frac{4\pi A}{P^2}, \quad K = \frac{\bar{\kappa} P}{2\pi}, \quad (8)$$

which both return unity for circles of any size.

In Fig. 7, we plot the different shape descriptors as a function of temperature comparing the Simple model with the more elaborate RawMD model. We see that an excellent agreement of cluster morphologies can be achieved using an effective bond strength of $E_B = 235$ meV and an attempt rate of $\nu_0 = 0.25$ THz. The value of E_B is closest to the effective bond strengths for edge diffusion in the RawMD model as these are the most important transitions when it comes to cluster relaxation. However, using this small value for E_B the dissociation rate is increased in the Simple model, which would lead to a lower cluster density. To compensate for this, the attempt rate ν_0 is lower than the attempt rate for free diffusion in the RawMD model, which increases the cluster density to produce the correct cluster sizes. Variation of the model parameters from their optimal values can lead to significant differences in the shape descriptors.

D. Multilayer Growth

We now turn to the consecutive growth of multiple layers, for which experimental results are available. In particular, we consider the data published in Ref. 13. One quantity that can be extracted from scattering data is the average cluster density [32], which is plotted in Fig. 8 as a function of the mean film height measured in monolayers (ML, molecular exposure = $F/\bar{n} \times \text{time}$ with \bar{n} the density of a full monolayer). For the molecular flux F we now chose the same value as in Ref. 13 corresponding to 0.1 monolayers per minute (ML/min). Starting from a high value, the cluster density rapidly decays and shows oscillations with minima corresponding to the filling of a complete layer. Also shown are results from KMC simulations employing the optimal Simple model [cf. Sec. III C]. While the period of the oscillations is recovered, our simulations yield cluster densities that are consistently too small, with the discrepancy exceeding one order of magnitude in the first and second layer. Moreover, in contrast to the experimental data, the simulated peak density in each layer is roughly independent of time.

In the same paper Ref. 13, experimental results are reproduced numerically using a simplified KMC

model (no sublattices, no distinction between A and B steps). The parameters of that model disagree with the parameters obtained here (and in other studies): $E_{D,\text{Bommel}} = 540 \text{ meV}$ for the diffusion barrier compared to $E_D = 192 \text{ meV}$ and $E_{B,\text{Bommel}} = 130 \text{ meV}$ for the bond strength compared to $E_B = 235 \text{ meV}$ (we recall that the bare Girifalco potential yields $E_G = 277 \text{ meV}$). The reason for the different behaviors of cluster densities is revealed by comparing snapshots of the corresponding KMC simulations in Fig. 9: the simplified KMC simulations show many small clusters [Fig. 9a and Supplementary Video 1] while our model leads to the formation of a few large clusters [Fig. 9b and Supplementary Video 2]. Also the morphologies disagree, in the simplified model the clusters are round compared to triangular “star” shapes. This difference can mostly be attributed to neglecting the distinction between A/B type edge diffusion as well as the low value for the bond strength of 130 meV .

An import difference between the simulations and the experiments is that the later have been performed on mica ($\text{KAl}_3\text{Si}_3\text{O}_{12}\text{H}_2$) and not on a clean $\text{C}_{60}(111)$ surface as assumed in our simulations, which may lead to impurities and “grain boundaries”. Our KMC simulations include a mechanism that leads to such grain boundaries. Due to the use of two sublattices, different clusters do not merge in our model when initiated on different sublattices. This leads to grain boundaries between clusters, which persist in the following layers as observed in Fig. 9b and might explain the differences with the experiments: First, the diffusion barrier of C_{60} is increased, which yields a much larger peak cluster density in the first layer. Second, mica has a lattice constant of 0.5 nm , which is half that of the diameter of a C_{60} molecule. Clusters on different effective sublattices cannot coalesce and thus create grain boundaries, which increase the peak cluster density also in the following layers.

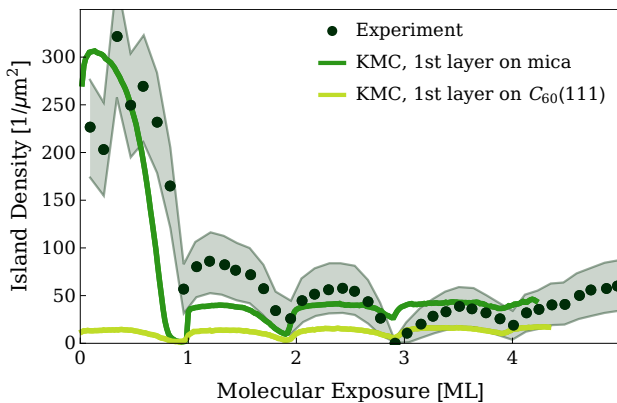


Figure 8. Cluster density as a function of molecular exposure (solid symbols) at $T = 333 \text{ K}$. Also plotted are results from the optimal Simple KMC model: unmodified model for growth on a clean C_{60} substrate (bright line) and with modified rates to reproduce the cluster density in the first layer (dark line).

To test this hypothesis, we have modified the dynamics for the first layer: no distinction between A and B type edge diffusion, an ascension barrier of $E_{A,\text{mica}} = 1150 \text{ meV}$ chosen large enough to guarantee layer-by-layer growth, and, most importantly, the diffusion barrier and attempt rate read

$$E_{D,\text{mica}} = 655 \text{ meV} \quad \nu_{0,\text{mica}} = 4 \times 10^{15} \text{ Hz}, \quad (9)$$

which have been determined through a parameter tuning to reproduce the experimental cluster densities in the first layer (data from Ref. 33). In Fig. 9c, we show the resulting temporal evolution of the film growth (see also Supplementary Video 3). It can be seen that the high cluster density of the first layer has a strong impact on the cluster densities of the subsequent layers because of the hindering effect of the grain boundaries on the diffusion process. Moreover, the time evolution of the cluster density is now in much better agreement with the experimental data at substrate temperature $T = 333 \text{ K}$ (Fig. 8, dark green line).

In Fig. 10, we plot the peak cluster density of the second layer as a function of substrate temperature. Interestingly, the experiment perfectly matches the result of the simulations using our Simple model without a modified first layer dynamics at the higher temperature $T = 353 \text{ K}$. At the lower temperature $T = 313 \text{ K}$, our simulations predict a minute increase while the experiments show an even stronger increase of the peak cluster density. To estimate the effect of the grain boundaries on the peak cluster density in the second layer, we have numerically determined (on a hexagonal lattice) the number of connected domains of initial clusters with $m = (1/0.5)^2 = 4$ different species. We find

$$n_{\text{domains}} \approx 0.38n_1, \quad (10)$$

where n_1 is the peak cluster density in the first layer. At the low temperature $T = 313 \text{ K}$, we find a good agreement of the experimental result with this prediction. This suggests that at low temperatures, cluster growth is indeed limited to domains enclosed by grain boundaries. At high temperatures, diffusion of C_{60} molecules can overcome these barriers and we recover the behavior on a clean C_{60} substrate.

IV. CONCLUSION

We have studied the epitaxial film growth of C_{60} molecules. Our central result is the systematic determination of a set of energy barriers (Table III) and attempt rates (Table IV) from many MD simulations of specific initial configurations. The bare rates do not obey detailed balance, which can be enforced through a single attempt rate ν_0 . A second simplification arises through employing a single effective bond energy E_B . We determine these two effective parameters through matching cluster morphologies, which yields

$$E_B = 235 \text{ meV}, \quad \nu_0 = 0.25 \text{ THz}. \quad (11)$$

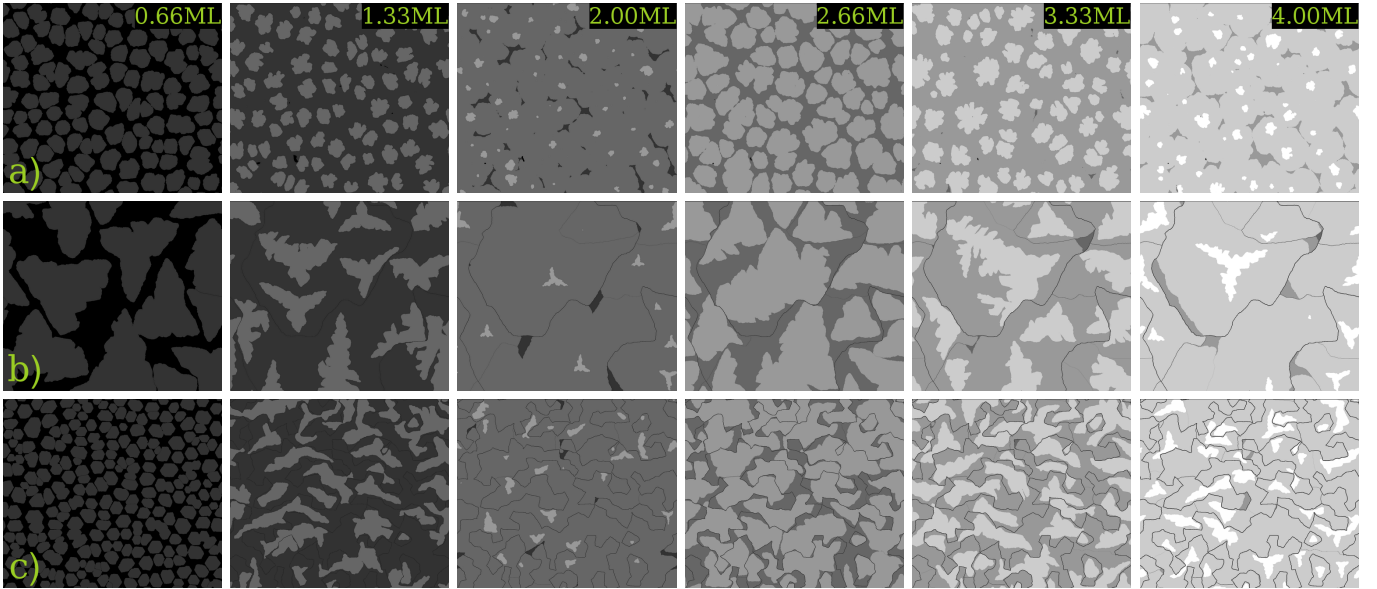


Figure 9. Snapshots at different stages of the multilayer growth simulations at a temperature of $T = 333$ K and a flux of $F = 0.1$ ML/min. (a) Simplified KMC model from Ref. 13. (b) Simple model derived in Sec. III C. Note [grain boundaries] (c) Using the Simple model for the second and higher layers. In the first layer, diffusion barrier and attempt rate have been altered to reproduce the experimental first layer cluster densities.

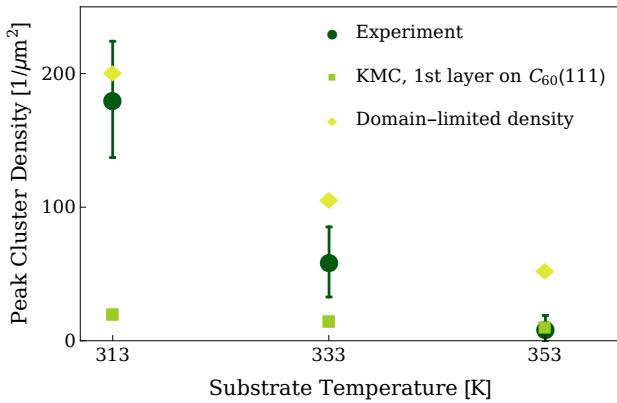


Figure 10. Peak cluster densities of the second C_{60} layer at the three experimentally observed temperatures (discs). Also shown are the KMC prediction of the optimal Simple model (diamonds) and the upper bound Eq. (10).

We have then investigated multilayer growth. Differences to the experimental results of Ref. 13 are attributed to the mica substrate, the smaller lattice constant of which might induce grain boundaries between growing clusters which limits their size and increases their number. It would be interesting to directly resolve morphologies in the experiments.

While the C_{60} on $C_{60}(111)$ system with the coarse-grained Girifalco potential is especially well suited, the method we have presented here to construct the rate parameters is generic and applicable to other combinations of organic molecule and substrate for which classical force fields are available. In particular, our results pave

the way to investigate more systematically the molecular dewetting of organic molecules on non-metallic substrates [34]. For more complex systems, the transition types and thus the number of parameters increases very quickly and might be prohibitively large to be determined from dedicated MD simulations. Another restriction on the part of the MD simulations is the feasibility of simulating the necessary timescales to observe the transitions of interest over a suitable range of temperatures. However, estimating rates can be achieved with less statistics and thus computational effort than spent here.

ACKNOWLEDGMENTS

We thank A. Kühnle for stimulating discussions. We acknowledge financial support by the Deutsche Forschungsgemeinschaft (grant no. 319880407). Numerical computations have been carried out on the MOGON II Cluster at ZDV Mainz.

Appendix A: Bond Counting

In KMC simulations of thin film growth it is common to use a bond counting approach [in our case Eq. (5)] to model energy barriers for transitions of particles that are in contact with a cluster.

Because of the short interaction range of C_{60} molecules, and supported by the results of Fig. 4, we decided to use the simplest version, which only considers the lateral nearest neighbors of the initial configuration.

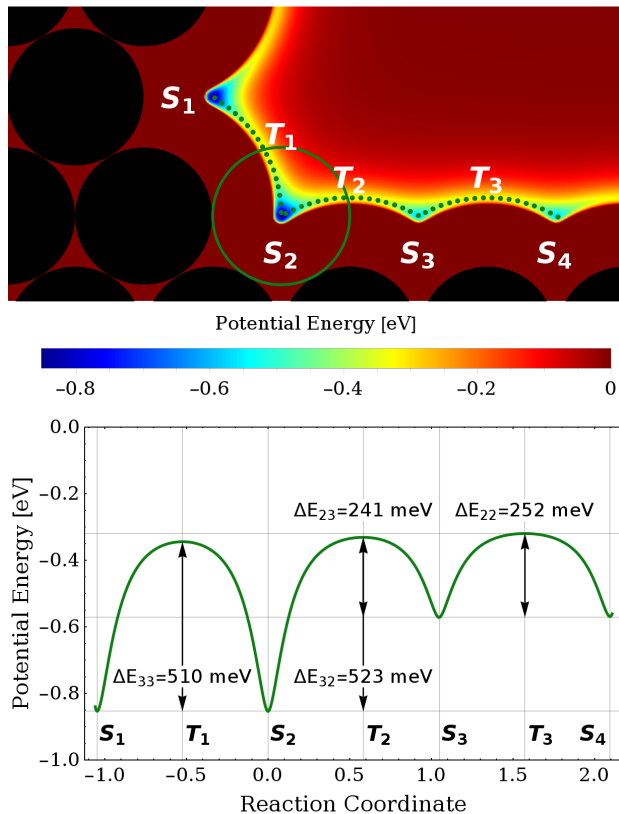


Figure 11. Top: Density plot of the potential energy of a sample molecule (dark green circle) in a given configuration of fixed cluster molecules (black disks, viewed from above) interacting via the Girifalco potential (the substrate is omitted). The dotted dark green line represents a possible reaction path connecting the four states S_1, \dots, S_4 passing through the transitional states T_1, T_2 and T_3 . Bottom: Plot of the potential energy along the dotted reaction path. The energy barriers ΔE_{ij} (i the number of initial neighbors, j the number of final neighbors) are only weakly affected by j .

How the short interaction range of the Girifalco potential justifies this approach is illustrated in Fig. 11. As an example, starting from the three neighbor (3N) initial state S_2 , the energy barriers for transition to the 3N final state S_1 or the 2N final state S_3 only have a negligible difference of 13 meV.

Appendix B: Mean cluster curvature

To calculate κ , we use the formula for the curvature of a continuous plane curve given in parametric form $\gamma(t) = (x(t), y(t))$,

$$\kappa(t) = \frac{|\dot{x}(t)\ddot{y}(t) - \ddot{x}(t)\dot{y}(t)|}{(\dot{x}(t)^2 + \dot{y}(t)^2)^{\frac{3}{2}}}. \quad (\text{B1})$$

As the cluster border is not given as a continuous curve, but by a set of N_E discrete border molecule positions, we approximate the derivatives at molecule n as finite differences

$$\dot{x}(n) = \frac{x(n+1) - x(n-1)}{2}, \quad (\text{B2})$$

$$\ddot{x}(n) = x(n+1) + x(n-1) - 2x(n) \quad (\text{B3})$$

(y coordinate analogous). Plugging these derivatives into Eq. (B1), we can calculate the mean border curvature via

$$\bar{\kappa} = \frac{1}{N_E} \sum_{n=1}^{N_E} \kappa(n). \quad (\text{B4})$$

-
- [1] A. H. Flood, J. F. Stoddart, D. W. Steuerman, and J. R. Heath, “Whence molecular electronics?” *Science* **306**, 2055–2056 (2004).
 - [2] M. Schulz, “The end of the road for silicon?” *Nature* **399**, 729–730 (1999).
 - [3] T. H. Ning, “Directions for silicon technology as we approach the end of CMOS scaling,” in *2010 10th IEEE International Conference on Solid-State and Integrated Circuit Technology* (2010) pp. 3–3.
 - [4] M. Graetzel, R. A. J. Janssen, D. B. Mitzi, and E. H. Sargent, “Materials interface engineering for solution-processed photovoltaics,” *Nature* **488**, 304–312 (2012).
 - [5] J. V. Barth, G. Costantini, and K. Kern, “Engineering atomic and molecular nanostructures at surfaces,” *Nature* **437**, 671–679 (2005).
 - [6] J. V. Barth, “Molecular architectonic on metal surfaces,” *Annu. Rev. Phys. Chem.* **58**, 375–407 (2007).
 - [7] A. Khnle, “Self-assembly of organic molecules at metal surfaces,” *Curr. Opin. Colloid Interface Sci.* **14**, 157–168 (2009).
 - [8] J. van der Lit, J. L. Marsman, R. S. Koster, P. H. Jacobse, S. A. den Hartog, D. Vanmaekelbergh, R. J. M. K. Gebbink, L. Filion, and I. Swart, “Modeling the self-assembly of organic molecules in 2D molecular layers with different structures,” *J. Phys. Chem. C* **120**, 318–323 (2016).
 - [9] H. Liu and P. Reinke, “C₆₀ thin film growth on graphite: Coexistence of spherical and fractal-dendritic islands,” *J. Chem. Phys.* **124**, 164707 (2006).
 - [10] B. R. Conrad, J. Tosado, G. Dutton, D. B. Dougherty, W. Jin, T. Bonnen, A. Schuldenfrei, W. G. Cullen, E. D. Williams, J. E. Reutt-Robey, and S. W. Robey, “C₆₀ cluster formation at interfaces with pentacene thin-film phases,” *Appl. Phys. Lett.* **95**, 213302 (2009).
 - [11] F. Loske, J. Lübke, J. Schütte, M. Reichling, and A. Kühnle, “Quantitative description of C₆₀ diffusion on an insulating surface,” *Phys. Rev. B* **82**, 155428 (2010).
 - [12] M. Körner, F. Loske, M. Einax, A. Kühnle, M. Reichling, and P. Maass, “Second-layer induced island morphologies in thin-film growth of fullerenes,” *Phys. Rev. Lett.* **107**,

- 016101 (2011).
- [13] S. Bommel, N. Kleppmann, C. Weber, H. Spranger, P. Schäfer, J. Novak, S. Roth, F. Schreiber, S. Klapp, and S. Kowarik, “Unravelling the multilayer growth of the fullerene C_{60} in real time,” *Nat. Commun.* **5**, 5388 (2014).
 - [14] A. Picone, D. Giannotti, M. Riva, A. Calloni, G. Bussetti, G. Berti, L. Du, F. Ciccacci, M. Finazzi, and A. Brambilla, “Controlling the electronic and structural coupling of C_{60} nano films on Fe(001) through oxygen adsorption at the interface,” *ACS Applied Materials & Interfaces* **8**, 26418–26424 (2016).
 - [15] M. Einax, W. Dieterich, and P. Maass, “Colloquium: Cluster growth on surfaces: Densities, size distributions, and morphologies,” *Rev. Mod. Phys.* **85**, 921–939 (2013).
 - [16] A. F. Voter, “Introduction to the Kinetic Monte Carlo Method,” in *Radiation Effects in Solids*, edited by K. E. Sickafus, E. A. Kotomin, and B. P. Uberuaga (Springer Netherlands, Dordrecht, 2007) pp. 1–23.
 - [17] D. T. Gillespie, “A general method for numerically simulating the stochastic time evolution of coupled chemical reactions,” *J. Comput. Phys.* **22**, 403–434 (1976).
 - [18] D. T. Gillespie, “Exact stochastic simulation of coupled chemical reactions,” *J. Phys. Chem.* **81**, 2340–2361 (1977).
 - [19] H. Liu, Z. Lin, L. V. Zhigilei, and P. Reinke, “Fractal structures in fullerene layers: Simulation of the growth process,” *J. Phys. Chem. C* **112**, 4687–4695 (2008).
 - [20] N. Kleppmann and S. H. L. Klapp, “Particle-resolved dynamics during multilayer growth of C_{60} ,” *Phys. Rev. B* **91**, 045436 (2015).
 - [21] Y. M. Acevedo, R. A. Cantrell, P. G. Berard, D. L. Koch, and P. Clancy, “Multiscale simulation and modeling of multilayer heteroepitactic growth of C_{60} on pentacene,” *Langmuir* **32**, 3045–3056 (2016).
 - [22] N. Kleppmann, F. Schreiber, and S. H. L. Klapp, “Limits of size scalability of diffusion and growth: Atoms versus molecules versus colloids,” *Phys. Rev. E* **95**, 020801 (2017).
 - [23] J. E. Goose, E. L. First, and P. Clancy, “Nature of step-edge barriers for small organic molecules,” *Phys. Rev. B* **81**, 205310 (2010).
 - [24] R. A. Cantrell and P. Clancy, “A new kinetic monte carlo algorithm for heteroepitactical growth: Case study of C_{60} growth on pentacene,” *J. Chem. Theory Comput.* **8**, 1048–1057 (2012).
 - [25] S. Plimpton, “Fast parallel algorithms for short-range molecular dynamics,” *J. Comput. Phys.* **117**, 1 – 19 (1995).
 - [26] L. A. Girifalco, “Molecular properties of fullerene in the gas and solid phases,” *J. Phys. Chem.* **96**, 858–861 (1992).
 - [27] L. A. Girifalco, “Interaction potential for C_{60} molecules,” *J. Phys. Chem.* **95**, 5370–5371 (1991).
 - [28] C. Chiutu, A. M. Sweetman, A. J. Lakin, A. Stannard, S. Jarvis, L. Kantorovich, J. L. Dunn, and P. Moriarty, “Precise orientation of a single C_{60} molecule on the tip of a scanning probe microscope,” *Phys. Rev. Lett.* **108**, 268302 (2012).
 - [29] A. N. Khlobystov, D. A. Britz, A. Ardavan, and G. A. D. Briggs, “Observation of ordered phases of fullerenes in carbon nanotubes,” *Phys. Rev. Lett.* **92**, 245507 (2004).
 - [30] P. A. Graviil, M. Devel, P. Lambin, X. Bouju, C. Girard, and A. A. Lucas, “Adsorption of C_{60} molecules,” *Phys. Rev. B* **53**, 1622–1629 (1996).
 - [31] U. Seifert, “Entropy production along a stochastic trajectory and an integral fluctuation theorem,” *Phys. Rev. Lett.* **95**, 040602 (2005).
 - [32] G. Renaud, R. Lazzari, C. Revenant, A. Barbier, M. Noblet, O. Ulrich, F. Leroy, J. Jupille, Y. Borensztein, C. R. Henry, J.-P. Deville, F. Scheurer, J. Mane-Mane, and O. Fruchart, “Real-time monitoring of growing nanoparticles,” *Science* **300**, 1416–1419 (2003).
 - [33] S. Bommel, *Unravelling nanoscale molecular processes in organic thin films*, Ph.D. thesis, Humboldt-Universität zu Berlin, Mathematisch-Naturwissenschaftliche Fakultät (2015).
 - [34] P. Rahe, R. Lindner, M. Kittelmann, M. Nimmrich, and A. Kühnle, “From dewetting to wetting molecular layers: C_{60} on $CaCO_3(10\bar{1}4)$ as a case study,” *Phys. Chem. Chem. Phys.* **14**, 6544–6548 (2012).